

# The Integrated Research Facility at Fort Detrick is Poised for the Future of Infectious Disease Imaging

Hui Wang<sup>1</sup>, Jeffrey Solomon<sup>2</sup>, Marcelo Castro<sup>1</sup>, Venkatesh Mani<sup>1</sup>, Ian Crozier<sup>2</sup>, Jens H Kuhn<sup>1</sup>, Anya Crane<sup>1</sup>, Claudia Calcagno Mani<sup>1, #</sup>

<sup>1</sup> Integrated Research Facility at Fort Detrick, Division of Clinical Research, National Institute of Allergy and Infectious Diseases, National Institutes of Health, Fort Detrick, Frederick, MD, USA

<sup>2</sup> Clinical Monitoring Research Program Directorate, Frederick National Laboratory for Cancer Research, Frederick, MD, USA

# Correspondence to: [claudia.mani@niaid.nih.gov](mailto:claudia.mani@niaid.nih.gov)

## Abstract

*In vivo* imaging is rapidly becoming a fundamental tool for the non-invasive longitudinal assessment of infectious diseases, including those caused by high-consequence viral pathogens such as Ebola, Lassa, and Nipah viruses. The Integrated Research Facility at Fort Detrick (IRF-Frederick) is an animal biosafety level 4 (ABSL-4) laboratory uniquely equipped with an array of clinical and pre-clinical imaging scanners that provide extensive multi-modality capabilities. Included are magnetic resonance imaging (MRI), positron emission tomography (PET), single-photon emission computed tomography (SPECT), and computed tomography (CT). Deployment of these imaging capabilities in the ABSL-4 setting enables the provision of standard as well as *de novo* development of qualitative and quantitative structural and functional imaging readouts in several animal models of high-consequence infectious diseases.

The IRF-Frederick's *in vivo* imaging of rodents and nonhuman primates focuses on the development, validation, and application of image acquisition and analysis protocols tailored to the investigation of high-consequence viral pathogens, including the disease characterization and evaluation of efficacy of medical countermeasures. Imaging work is performed in synergy with other IRF-Frederick scientific resources—aerobiology, drug screening, comparative medicine, genomics, immunology, molecular virology, and pathology. In order to achieve these goals, the imaging team performs (1) morphological and functional MR and CT imaging to evaluate changes in organ function after infection; (2) molecular MR and PET imaging of host responses and organ damage; (3) qualitative and semi-quantitative image analysis; and (4) sophisticated artificial-intelligence image analysis methods from algorithms based on conventional machine learning and deep learning.

The IRF-Frederick has continued to leverage its imaging capabilities to investigate the natural history and disease mechanisms after exposure to high-consequence Risk Group 4 pathogens. The coronavirus disease 2019 (COVID-19) pandemic required an urgent pivot to include imaging of animals after severe acute respiratory syndrome coronavirus 2 (SARS-CoV-2) exposure (Figure 1). In the near future, the IRF-Frederick will further expand its pre-clinical imaging capabilities by

acquiring additional multi-modality small, medium, and large PET, CT, SPECT, and optical imaging capabilities that will further aid in the characterization of emerging infectious diseases.

### **Selected Publications**

Finch, C. L., I. Crozier, J. H. Lee, R. Byrum, T. K. Cooper, J. Liang, K. Sharer, J. Solomon, P. J. Sayre, G. Kocher, C. Bartos, N. M. Aiosa, M. Castro, P. A. Larson, R. Adams, B. Beitzel, N. Di Paola, J. R. Kugelman, J. R. Kurtz, T. Burdette, M. C. Nason, I. M. Feuerstein, G. Palacios, M. C. St Claire, M. G. Lackemeyer, R. F. Johnson, K. M. Braun, M. D. Ramuta, J. Wada, C. S. Schmaljohn, T. C. Friedrich, D. H. O'Connor, and J. H. Kuhn. 2020. '**Characteristic and quantifiable COVID-19-like abnormalities in CT- and PET/CT-imaged lungs of SARS-CoV-2-infected crab-eating macaques (*Macaca fascicularis*)**', bioRxiv.

Lee, J. H., D. A. Hammoud, Y. Cong, L. M. Huzella, M. A. Castro, J. Solomon, J. Laux, M. Lackemeyer, J. K. Bohannon, O. Rojas, R. Byrum, R. Adams, D. Ragland, M. St Claire, V. Munster, and M. R. Holbrook. 2020. '**The Use of Large-Particle Aerosol Exposure to Nipah Virus to Mimic Human Neurological Disease Manifestations in the African Green Monkey**', *J Infect Dis*, 221: S419-S30.

Schreiber-Stainthorp, W., J. Solomon, J. H. Lee, M. Castro, S. Shah, N. Martinez-Orengo, R. Reeder, D. Maric, R. Gross, J. Qin, K. R. Hagen, R. F. Johnson, and D. A. Hammoud. 2021. '**Longitudinal in vivo imaging of acute neuropathology in a monkey model of Ebola virus infection**', *Nat Commun*, 12: 2855.

Shah, S., S. Sinharay, R. Patel, J. Solomon, J. H. Lee, W. Schreiber-Stainthorp, F. Basuli, X. Zhang, K. R. Hagen, R. Reeder, P. Wakim, L. M. Huzella, D. Maric, R. F. Johnson, and D. A. Hammoud. 2022. '**PET imaging of TSPO expression in immune cells can assess organ-level pathophysiology in high-consequence viral infections**', *Proc Natl Acad Sci U S A*, 119: e2110846119.

Reza, S. M. S., D. Bradley, N. Aiosa, M. Castro, J. H. Lee, B. Y. Lee, R. S. Bennett, L. E. Hensley, Y. Cong, R. Johnson, D. Hammoud, I. Feuerstein, and J. Solomon. 2021. '**Deep Learning for Automated Liver Segmentation to Aid in the Study of Infectious Diseases in Nonhuman Primates**', *Acad Radiol*, 28 Suppl 1: S37-S44.

Solomon, J., N. Aiosa, D. Bradley, M. A. Castro, S. Reza, C. Bartos, P. Sayre, J. H. Lee, J. Sword, M. R. Holbrook, R. S. Bennett, D. A. Hammoud, R. F. Johnson, and I. Feuerstein. 2020. '**Atlas-based liver segmentation for nonhuman primate research**', *Int J Comput Assist Radiol Surg*, 15: 1631-38.

Chefer, S., J. Seidel, A. S. Cockrell, B. Yount, J. Solomon, K. R. Hagen, D. X. Liu, L. M. Huzella, M. R. Kumar, E. Postnikova, J. K. Bohannon, M. G. Lackemeyer, K. Cooper, A. Endlich-Frazier, H. Sharma, D. Thomasson, C. Bartos, P. J. Sayre, A. Sims, J. Dyllal, M. R. Holbrook, P. B. Jahrling, R. S. Baric, and R. F. Johnson. 2018. '**The Human Sodium Iodide Symporter as a Reporter Gene for Studying Middle East Respiratory Syndrome Coronavirus Pathogenesis**', *mSphere*, 3.

Dyllal, J., R. F. Johnson, S. Chefer, C. Leyson, D. Thomasson, J. Seidel, D. R. Ragland, R. Byrum, C. Jett, J. A. Cann, M. St Claire, E. Jagoda, R. C. Reba, D. Hammoud, J. E. Blaney, and P. B. Jahrling. 2017. '**[(18)F]-Fluorodeoxyglucose Uptake in Lymphoid Tissue Serves as a Predictor of Disease Outcome in the Nonhuman Primate Model of Monkeypox Virus Infection**', *J Virol*, 91.

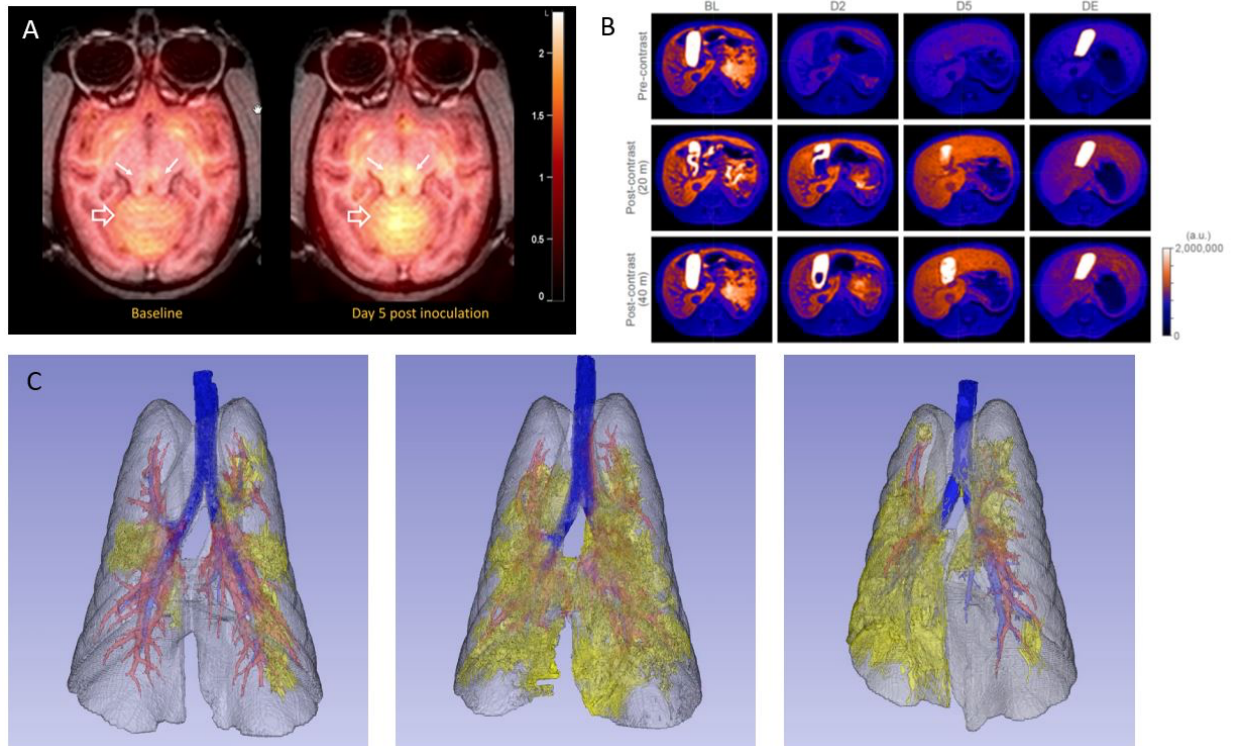


Figure 1. Representative *in vivo* imaging studies of nonhuman primates. (A) Rhesus macaques were inoculated with 1,000 plaque forming units of Ebola virus (EBOV), Makona isolate, via intramuscular injection. Serial 2-deoxy-2-[fluorine-18]fluoro-D-glucose ( $^{18}\text{F}$ -FDG) positron emission tomography (PET) computed tomography (CT) scans were performed at baseline, 2 d, 5 d, and 7/8 d post-exposure. Representative parametric relative standardized uptake value (SUV) maps showed increased  $^{18}\text{F}$ -FDG uptake in the brainstem (solid white arrows) and cerebellum (open white arrows) on Day 5 compared to baseline [*Nat Commun*, 2021 May 17;12(1):2855]. (B) Longitudinal contrast-enhanced magnetic resonance imaging (MRI) showed liver damage in EBOV-exposed crab-eating macaques. (C) 3D reconstruction and visualization of the varied extent and temporal evolution of the bilateral, multi-lobar pulmonary abnormalities in three different macaques at 2 d (left), 4 d (middle), and 6 d after exposure to SARS-CoV-2. Blue = airway, red = vessels, yellow = lesion, 3D, three-dimensional. (*bioRxiv preprint doi: <https://www.biorxiv.org/content/10.1101/2020.05.14.096727v1>*)

## MRI of Liver Inflammation Using an Oxidatively Activated Imaging Probe

Mozhdeh Sojoodi<sup>1</sup>, Veronica Clavijo Jordan<sup>2</sup>, Stephen Cole Barrett<sup>1</sup>, Kenneth K. Tanabe<sup>1</sup>, Peter Caravan<sup>2</sup>, Eric M. Gale<sup>2</sup>

<sup>1</sup> Department of Surgical Oncology, Massachusetts General Hospital/ Harvard Medical School, USA, <sup>2</sup> A. A. Martinos Center, Institute for Innovation in Imaging, and Department of Radiology

**Introduction:** Inflammation is a key factor in histologic scoring of many acute and chronic liver disease states, but clinical imaging tools to non-invasively diagnose liver inflammation or characterize inflammation disease activity are underdeveloped. The inflammatory liver microenvironment is aberrantly oxidizing due in part to reactive oxygen species (ROS) generated by myeloid leukocytes. We hypothesized that magnetic resonance imaging (MRI) using the oxidatively activated probe Fe-PyC3A will provide a noninvasive biomarker of liver inflammation.

**Methods:** A mouse model of drug-induced liver injury (DILI) was generated through i.p. injection of a hepatotoxic dose of acetaminophen (450 mg/kg), and control mice received the vehicle. T1-weighted images were acquired dynamically prior to and out to 25 minutes after i.v. injection of Fe-PyC3A. Liver tissue and serum collected from mice treated with vehicle or 450 mg/kg acetaminophen were analyzed by H&E, assayed for serologic markers of liver function, and for intrahepatic myeloperoxidase-positive cell content using IHC. Intrahepatic myeloid leukocyte content is determined by ex vivo flow cytometry assay and immunohistochemistry. Serum markers of liver function were correlated with the (post-pre)injection increase in liver vs muscle contrast-to-noise ratio observed a 2 min after Fe-PyC3A injection (DCNR<sub>2m</sub>).

**Results:** Serum analysis identified significantly elevated levels of liver injury markers including ALP, ALT, and AST in mice treated with acetaminophen compared to mice receiving vehicle consistent with DILI resulting from acetaminophen overdose. Flow cytometry data indicated that hepatic neutrophil infiltration was varied in both vehicle and acetaminophen treated mice and did not differ significantly between groups. Hepatic neutrophil content also correlated poorly with serum liver function markers. However, hepatic neutrophil content correlated positively and significantly with DCNR<sub>2m</sub> ( $r = 0.69$ ,  $P < 0.0001$ ). Strong enhancement was observed in liver tissue with high neutrophil content, and low or no signal enhancement was observed in liver tissue with low neutrophil content (**Figure 1**).

**Discussion:** Most acute and chronic liver disease states possess an inflammatory component, however non-invasive biomarkers for liver inflammation are lacking. Serologic markers offer limited information regarding liver inflammation disease activity and clinical imaging tools are underdeveloped. Our data indicate that Fe-PyC3A differentially generates positive MRI signal enhancement in inflamed liver tissue within 2 minutes of intravenous injection (**Figure 1A-C**). MR imaging using Fe-PyC3A was more sensitive to acute liver inflammatory changes than serologic markers commonly used to assess liver function (ALP, ALT, and AST). The DCNR<sub>2m</sub> values correlated positively and significantly with the varied levels of intrahepatic neutrophil content (**Figure 1D-G**). This finding simultaneously underscores the non-specificity of non-invasive clinical markers of liver inflammation and indicates how an oxidatively activated MR imaging probe such as Fe-PyC3A could be utilized to interrogate pathologic changes in inflammatory disease activity that are currently only measurable through invasive biopsy.

**Conclusion:** MR imaging using Fe-PyC3A merits further evaluation and development as a noninvasive biomarker of liver inflammation.

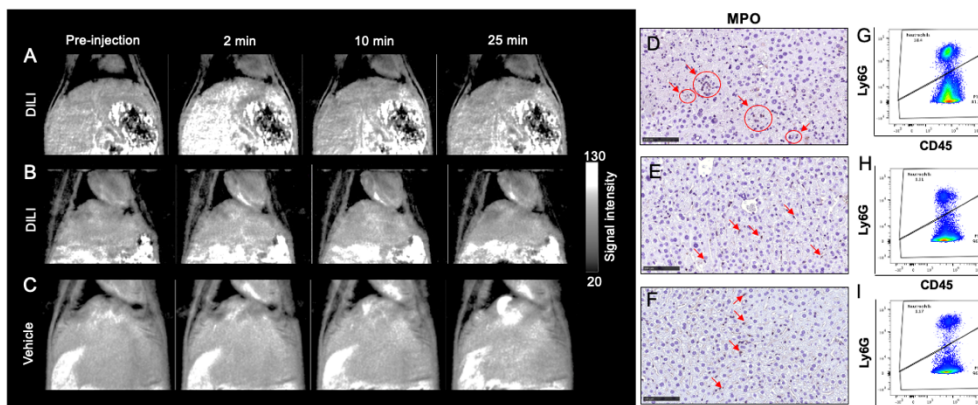


**Figure 1. Representative MR images and ex vivo from acetaminophen and vehicle treated mice exhibiting varied liver inflammatory response.** (A-C) Comparison of coronal T<sub>1</sub>-weighted abdominal images of mice receiving either a hepatotoxic dose of acetaminophen or vehicle i.p. recorded prior to, 2 min, 10 min, and 25 min after injection of 0.2 mmol/kg Fe-PyC3A. (D-H) Myeloperoxidase immunostaining (D-F) and flow cytometry dot plots showing Ly6G out of CD45 (ie. neutrophil percentage of live leukocytes) (G-I) corresponding to the mice shown in A-C, respectively.

# Development of Perfluorocarbon-encapsulated Polymer Nanoparticle for $^{19}\text{F}$ MRI Contrast Agents

○Yuki Konishi<sup>1</sup>, Fuminori Sugihara<sup>2,3</sup>, Masafumi Minoshima<sup>1</sup>, and Kazuya Kikuchi<sup>1,2</sup>

<sup>1</sup>Graduate School of Engineering, <sup>2</sup>Immunology Frontier Research Center, <sup>3</sup>Research Institute for Microbial Diseases, Osaka University, Osaka, Japan

**[Introduction]** MRI is widely used as a noninvasive in vivo imaging technique.  $^{19}\text{F}$  MRI has favorable NMR properties in 100% natural abundance of  $^{19}\text{F}$ , high NMR sensitivity, and no endogenous background signal in animal bodies. Therefore,  $^{19}\text{F}$  MRI probes are attracting in vivo imaging tools for tracking specific cells and imaging enzyme activities in deep tissues. We have developed a perfluorocarbon (PFC)-encapsulated silica nanoparticle, termed FLAME<sup>1)</sup> (FLUorine Accumulated silica nanoparticles for  $^{19}\text{F}$  MRI Enhancement). Silica nanoparticle-based nanoprobes enabled sensitive detection of  $^{19}\text{F}$  MRI signals in vivo and facile surface modifications for functionalization. However,  $^{19}\text{F}$  MRI signal of silica nanoparticle FLAME remains in liver and spleen for a long time after intravenous injection in mice, indicating accumulation of silica nanoparticle in these tissues.

Soft nanomaterials such as nanogels are attractive materials for DDS (Drug Delivery System) because they have elasticity and high tissue penetration ability through deformation. Hui *et al.* reported that soft nanoparticles penetrate the deep tissue of the tumor sphere<sup>2)</sup>. Then, we hypothesized soft polymer nanoparticles can penetrate the tissue and undergo more rapid clearance from the body than silica nanoparticles.

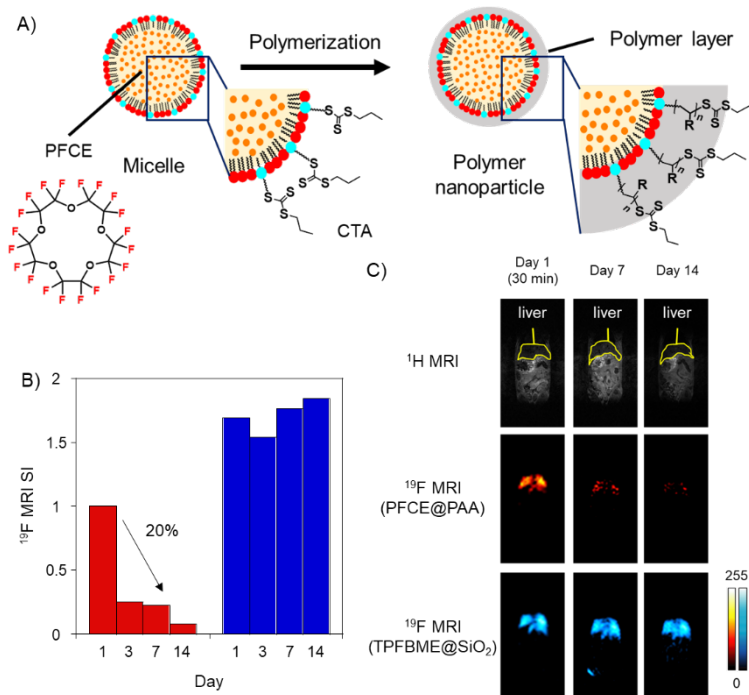
In this research, we developed PFC-encapsulated polymer nanoparticles as a  $^{19}\text{F}$  MRI contrast agent to avoid long-term accumulation in the body. This nanoparticle was covered with polymer layer instead of silica. The nanoparticles were prepared by RAFT (Reversible Addition Fragmentation chain Transfer) polymerization on PFC-encapsulated micelles. RAFT polymerization is one of living radical polymerization and proceeds under various conditions such as in water or on lipid membrane.

**[Methods and Results]** We prepared nanomicelles encapsulated PFCE (perfluoro-15-crown-5 ether) having 20 equivalent  $^{19}\text{F}$  atoms. Acrylic acid, a cross-linker, a fluorophore (rhodamine derivative), and an initiator were then added to the nanomicelles. The polymerization on the micelle proceeded to obtain nanoparticles with approximately 160 nm-size (Figure 1A).  $^{19}\text{F}$  NMR spectrum showed PFCE (core compound) was encapsulated in the nanoparticle without shortening transverse relaxation time ( $T_2$ ). Further, high-speed AFM (Atomic Force Microscopy) measurement confirmed the elasticity of the polymer nanoparticles. Next, we compared accumulated amounts in mouse liver between polymer and silica nanoparticles by multicolor  $^{19}\text{F}$  MRI<sup>4)</sup>. PFCE-encapsulated polymer nanoparticle (PFCE@PAA) and TPFBME (1,1,1-tris(perfluoro-*tert*-butoxymethyl)ethane)-encapsulated silica nanoparticle (TPFBME@SiO<sub>2</sub>) were prepared and administrated into a mouse simultaneously. The  $^{19}\text{F}$  MR signal from both nanoparticles was observed from the liver after injection of nanoparticles. The  $^{19}\text{F}$  MRI signal intensity from silica nanoparticle did not change over two weeks. However, the intensity from polymer nanoparticle decreased to 20% after seven days and 8% 2 weeks (Figure 1B, C).

**[Conclusion]** We conclude that the polymer nanoparticle underwent more rapid clearance than silica nanoparticle, indicating the suppression of long-term accumulation in the liver.

**[References]** 1) H. Matsushita, *Angew. Chem. Int. Ed.* **2014**, *53*, 1008. 2) Y. Hui *et al.*, *ACS Nano* **2018**, *12*, 2846. 3) T. Uchihashi *et al.*, *Biophys. Rev.* **2020**, *12*, 363. 4) K. Akazawa *et al.*, *Angew. Chem. Int. Ed.* **2018**, *57*, 16742.

**Figure 1.** A) Scheme of polymerization on the surface of PFCE-encapsulated micelle. B)  $^{19}\text{F}$  MR signal intensity of nanoparticles. Normalized by the SI (signal intensity) of the polymer nanoparticle on Day 1. SI = area  $\times$  mean. C)  $^1\text{H}$  and  $^{19}\text{F}$  MR images of a mouse administrated nanoparticles.



# DNA Origami Voltage Sensitive Contrast Agents for MRI

Benjamin Cary<sup>1</sup>, Grigory Tikhomirov<sup>1</sup>

1) University of California, Berkeley EECS Department  
bencary@berkeley.edu

One mechanism by which neurons transmit information is through action potentials. Researchers have developed extensive tools for probing these signals. However, these tools require invasive methods as direct access to the neurons is usually needed. Other non-invasive methods such as functional magnetic resonance imaging (fMRI), electroencephalography and magnetoencephalography are used in labs and clinics, but they sacrifice spatial and temporal resolution in order to be non-invasive. Genetically encoded voltage indicators (GEVIs) are an optical method for quantifying electrical signals and they achieve high spatial and temporal resolution. They are highly invasive as photon sensors need to be adjacent to the neurons as optical frequencies of light scatter in tissue. A method which could non-invasively elucidate electrical signals without the pitfalls of GEVIs would be a useful tool for neuroscientists and clinicians. In this poster we will describe a design of a nanoscale DNA origami contrast agent for leveraging MRI's non-invasiveness to create such a tool. By integrating the established methods of DNA nanopores, DNA electric-field linear shuttles, and synthetic nanoparticle constructs used in magnetic resonance tuning, we have modeled a device which can respond to sub-millisecond changes in neuron membrane potentials. We also present potential MR readout schemes to measure the average change in contrast across tens of milliseconds associated with neuronal activity in a voxel. Experimental validation is forthcoming.

# Clickable perfluorocarbon nanoemulsion for $^{19}\text{F}$ MRI and macrophage subtype detection

Junhan Zhou<sup>1</sup>, Adam S. Perez<sup>1</sup>, Benjamin Leach<sup>2</sup>, Xingjian Yu<sup>1</sup>, Hongyan Xu<sup>2</sup>, Deanne Lister<sup>2</sup>, Stephen R. Adams<sup>3</sup>, Kit S. Lam<sup>1,5,6,7</sup>, Eric T. Ahrens<sup>2</sup>, Angelique Y. Louie<sup>1,4</sup>

<sup>1</sup> Chemistry Graduate Group, University of California, Davis, CA, 95616, USA

<sup>2</sup> Department of Radiology, University of California, San Diego, La Jolla, CA 92093, USA

<sup>3</sup> Department of Pharmacology, University of California, San Diego, La Jolla, CA 92093, USA

<sup>4</sup> Department of Biomedical Engineering, University of California Davis, Davis, CA 95616, USA

<sup>5</sup> Department of Biochemistry and Molecular Medicine, University of California, Davis, CA, 95616, USA

<sup>6</sup> Comprehensive Cancer Center, University of California, Davis, CA, 95616, USA

<sup>7</sup> Division of Hematology & Oncology, Department of Internal Medicine, University of California, Davis, CA, 95616, USA

**Introduction** The complexity of the macrophage response to diseases and crucial metabolic events has only recently been appreciated, and it is now understood that macrophages polarize between functions that inhibit or promote disease. Increasingly, distinct macrophage subtypes have been associated with disease progression or resolution. We introduce an *in vivo* imaging probe platform that is readily modifiable to accommodate binding of different molecular targeting moieties and payloads for multi-modal image generation. Uptake of the fluorescent PFC by macrophages was demonstrated *in situ* in an acute inflammation mouse model, where fluorescence imaging and  $^1\text{H}/^{19}\text{F}$  MRI was used for *in vivo* detection. Further, we perform macrophage subtype uptake studies *in vitro* to assess the capability of macrophage subtype detection.

**Methods** *Synthesis and in vivo MRI imaging for fluorescent PFC were reported as previous publication.*<sup>1</sup> ***In vitro* macrophage subtype uptake study** We modified the NE formula of DBCO-NE for macrophage subtype targeting by adding 3 mol% of PEG300-DSPE and 2 mol% DBCO-PEG600-DSPE during the nanoemulsification process to obtain DBCO-PEG-NE, and a PEG-NE with 5 mol% PEG300-DSPE was also synthesized as a control. A Synthetic peptide (NP31, CMSYEGSWRKWVMWGGC) with nanomolar affinity for CD40 was synthesized using peptide synthesizer. THP-1 cells were cultured and plated into 6-well culture plates at a density of 800,000 cell/well in RPMI supplemented with 10% FBS, 2% penicillin/streptomycin, 2 mM L-glutamine. Cells were stimulated with 10  $\mu\text{g}/\text{mL}$  PMA for 48 hours at 37°C (5%  $\text{CO}_2$ ) and polarized with cytokines under either M1 phenotype conditions 0.3ng/mL LPS, 1 ng/mL IFN- $\gamma$ , or M2 phenotype conditions 20 ng/mL IL-4 and IL-13 for 24h. Solutions of 8mg/mL of PFCE of NP31-DBCO-NE and PEG-NE were prepared and added to cells for 1 hour at 37°C. Cells were then washed 3 times with PBS, counted, then lysed using deionized water (freeze, thaw). The cell lysates were assessed by  $^{19}\text{F}$ -NMR for cellular uptake.

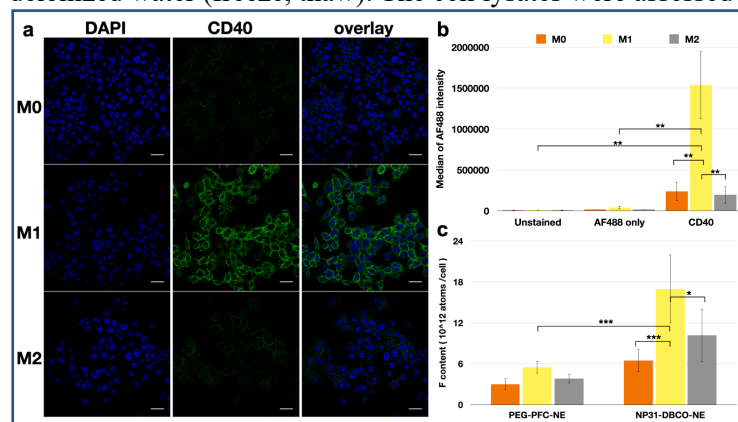


**Figure 1.** Macrophages subtype uptake *in vitro*. a. Representative immunofluorescence images for CD40 staining on polarized THP-1 derived macrophages. The cell nuclei were counterstained with Hoechst 33342. Scale bar = 30  $\mu\text{m}$ . b. Flow cytometry for assessing CD40 surface expression on polarized THP-1 derived macrophages. Unstained cells and AF488 secondary only stained cells were measured as control of auto-fluorescence. c. Quantitative cellular uptake efficiency of polarized THP-1 derived macrophages by  $^{19}\text{F}$ -NMR. The differences were considered significant with p values  $* < 0.05$ ,  $** < 0.01$ , and  $*** < 0.001$  as shown.

**Results and discussion** We demonstrate the utility of perfluorocarbon (PFC) nanoemulsions incorporating dibenzocyclooctyne (DBCO) enabling functionalization, post-emulsification, via click-reaction with azide-containing ligands. Addition of DBCO-lipid to the surfactant in PFC nanoemulsions did not affect nanoemulsion size or nanoemulsion stability. As proof-of-concept, fluorescent dye-azides were conjugated to PFC nanoemulsions, demonstrating the feasibility of functionalization by click reaction. Overall, these data demonstrate the potential of PFC nanoemulsions incorporating DBCO as a versatile platform for generating functionalized probes. Further, we exam the capability of macrophage subtype detection using NP31 clicked PFC nanoemulsions *in vitro* for CD40 targeting. CD40 receptor protein expression level for polarized THP-1 derived macrophage were assessed by immunofluorescent staining and flow cytometry (Figure a and b). M1 polarized macrophage showed significantly higher CD40 expression compared to M0 and M2 polarized macrophages. Polarized macrophages uptake efficiency was determined

by  $^{19}\text{F}$ -NMR to quantify F atoms per cell (Figure c). M1 polarized macrophages showed significantly higher uptake of NP31-DBCO-NE compared to same dose of PEG-NE. Importantly, M1 polarized macrophages showed significantly higher uptake compared to M0 and M2 polarized macrophages. No significant differences for cell uptake were found for M0 and M2 polarized macrophages treated with same dose of NP31-DBCO-NE and PEG-NE. The cellular uptake data is correlated with the CD40 expression, which suggests that NP31-DBCO-NE is promising for future macrophage subtype detection *in vivo* imaging study.

**References** 1) Perez, A. S. *et al.* Click-Ready Perfluorocarbon Nanoemulsion for  $^{19}\text{F}$  MRI and Multimodal Cellular Detection. *ACS Nanosci. Au* (2021). doi:10.1021/acsnanoscienceau.1c00016

### Molecular MRI can detect accumulation of CAR T-cells in GBM

Wei Wu<sup>1,2</sup>, Edwin Chang<sup>1</sup>, Linchun Jin<sup>3</sup>, Shiqin Liu<sup>1</sup>, Ching-Hsin Huang<sup>1</sup>, Rozy Kamal<sup>1</sup>, Nour Mary Aissaoui<sup>1</sup>, Laura Pisani<sup>1</sup>, Michael Moseley<sup>1</sup>, Tanya Stoyanova<sup>1</sup>, Ramasamy Paulmurugan<sup>1</sup>, Jianping Huang<sup>3</sup>, Duane A. Mitchell<sup>3</sup> and Heike E. Daldrup-Link<sup>1,4</sup>

1. Department of Radiology, Molecular Imaging Program at Stanford, Stanford University, Stanford, CA, USA. 2. Institute of Stem Cell Research and Regenerative Medicine, Stanford University, Stanford, CA, USA. 3. Lillian S. Wells Department of Neurosurgery, University of Florida, Gainesville, FL, USA. 4. Department of Pediatrics, Stanford University School of Medicine, Stanford, CA, USA

**INTRODUCTION:** Glioblastoma multiforme (GBM) is the most malignant brain tumor with 5-year survival of 7.2% in the United States<sup>1</sup>. The cancer is highly heterogeneous with regular tumor relapse<sup>2</sup>. Chimeric Antigen Receptor (CAR) T-Cells can be genetically modified to express surface ligands that target molecular surface markers on brain cancers<sup>3</sup>. CAR T-Cell therapy has induced measurable response in patients with leukemia and lymphoma. However, CAR T-cell therapy alone has been ineffective in GBM due to its highly immunosuppressive microenvironment. X-ray irradiation can render GBM receptive to immunotherapy<sup>4</sup>. The absence of a clinically viable tracking technique for CAR T-cells has been recognized as a main hurdle to optimize CAR T-cell therapy for GBM. MegaPro is an iron oxide nanoparticle which has passed a phase 2 clinical trial as an MRI contrast agent. By exploiting clinically translatable iron oxide nanoparticles, such as MegaPro, this study employs the modalities of magnetic resonance imaging (MRI) and magnetic particle imaging (MPI) for the *in vivo* tracking of CAR T-cells into preclinical models of glioblastomas. **METHOD:** Human U87-MG/eGFP-fLuc GBM were intracranially implanted into 10 NRG mice. Bioluminescence imaging (BLI) was used to monitor tumor growth. When the tumors had reached a total luminescent flux of  $5 \times 10^8$  photons/second, animals received two fractionated irradiations (4.5Gy each) of the whole brain. CD70CAR (8R-70CAR) T-cells and untargeted T-cells were labeled with MegaPro iron oxide nanoparticles and were intracardiacally injected to 5 mice, respectively at day 7 after the irradiation, followed by serial BLI, MRI and MPI on day 1, 3 and 5 after the injection. **RESULTS:** 5 days after administration T-cells, the tumor MRI signal showed a significant decline in the group treated with nanoparticle labeled CAR T-cells but not in untargeted T-cells treated group (Figure. 1A). The T2\* relaxation time of GBM treated with iron-labeled CAR T-cells significantly decreased from  $25.75 \pm 2.13$  ms at baseline (i.e. after irradiation but before treatment) to  $12.35 \pm 1.06$  ms on day 5 post-treatment ( $P < 0.001$ ). T2\* relaxation time of GBM treated with iron-labeled untargeted T-cells was not significantly different between baseline ( $24.44 \pm 1.15$  ms) and 5 days post-treatment ( $22.32 \pm 0.58$ ms) ( $P > 0.05$ ). Similarly, MPI demonstrated a significant increase in MPI signal of GBM on day 5 ( $17.66 \pm 2.85$ ug) after injection of iron oxide labeled CAR T-cells compared to baseline values ( $0.74 \pm 0.36$  ug) ( $P < 0.001$ ). By comparison, the MPI signal of GBM treated with iron-labeled untargeted T-cells were significantly lower than for the mice treated with labeled CAR T-cells on each day ( $p < 0.001$ ). **DISCUSSION:** Our data show that MegaPro-NP can be used for *in vivo* tracking of CAR T-cells in a preclinical animal model of GBM. There is an immediate need for a diagnostic tool that can noninvasively quantify the accumulation of CAR T-cells in brain cancers. Real-time *in vivo* cell tracking could provide objective information on CAR T-cell distribution in the tumor and normal brain tissue, which

could inform early interventions to improve anti-tumor efficacy or reduce side effects. Our findings have broad implications. The described nanoparticle labeling approach could be readily translated to the clinic because the underlying iron oxide nano particles are readily clinically available, and MRI is the technique of choice for brain tumor imaging in patients. Our imaging technique could provide insights on CAR T-cell penetration into tumors and visualize potential off-target effects.

**CONCLUSION:** This study demonstrates the successful and specific tracking of CD70CAR (8R-70CAR) T-cells in preclinical glioblastoma model through clinically translatable imaging technologies (MRI and MPI), which can be significant tools in the development and monitoring of effective CAR T-cell therapy.

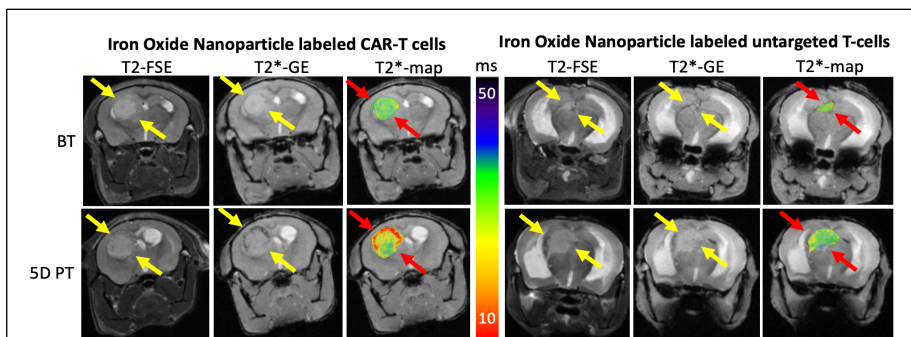


**Figure 1:** MRI scanning showed a significant decline of the tumor T2-signal after treatment with nanoparticle labeled CD70CAR (8R-70CAR) T-cells. T2-weighted fast spin echo (FSE), T2\* multi-gradient echo (MGE), and T2\*-GE fused with superimposed color-coded T2\* maps demonstrating the infiltration of CAR T-cells. Mice treated with labeled CAR T-cells, and with untargeted T-cells on U87-MG/GFP-Luc xenografts before treatment (BT) and 5 days post treatment (5D PT).

**REFERENCES:** 1. Ostrom QT, et al: CBTRUS Statistical Report: Primary Brain and Other Central Nervous System Tumors Diagnosed in the United States in 2013-2017. *Neuro Oncol* 2020,2:iv1-iv96. 2. Ringel F, et al (2016). Clinical benefit from resection of recurrent glioblastomas: results of a multicenter study including 503 patients with recurrent glioblastomas undergoing surgical resection. *Neuro Oncol* 18, 96–104. 3. Land CA, et al: Chimeric antigen receptor T-cell therapy in glioblastoma: charging the T cells to fight. *J Transl Med* 2020, 18:428. 4. Jin L, et al: CXCR1- or CXCR2-modified CAR T cells co-opt IL-8 for maximal antitumor efficacy in solid tumors. *Nat Commun* 2019, 10:4016.

## Structure-function study of Eu-based contrast agents toward measuring hypoxia and solid-phase cryptand synthesis

Alexander G. Sertage,<sup>1</sup> Brooke A. Corbin,<sup>1</sup> S. A. Amali S. Subasinghe,<sup>1</sup> and Matthew J. Allen<sup>1</sup>

<sup>1</sup>Department of Chemistry, Wayne State University, Detroit, Michigan 48202, USA

**Introduction:** Hypoxia is relevant to several diseases, resulting in many efforts being pursued to image hypoxia.<sup>1-2</sup> However, it is difficult to noninvasively detect hypoxia due to the limitations of probes needed for in vivo imaging modalities.<sup>3</sup> One promising class of probes for imaging hypoxia are europium-containing complexes that enhance contrast in magnetic resonance imaging as a function of the oxidation state of europium.<sup>4-7</sup> Further, the ability to change the oxidation state of europium can be controlled using coordination chemistry. Two issues associated with the current class of europium-containing complexes are the question of the mechanism of response for F-containing ligands and difficult purifications associated with cryptands. To address these issues, we are synthesizing ligands that contain fluorine atoms in different patterns to determine the mechanistic qualities of the 12-fluorine contrast agent that enable imaging of hypoxia in vivo. Additionally, cryptands are being synthesized using solid-phase techniques to avoid multiple purification steps associated with their solid-phase synthesis.

**Methods:** Fluorine-containing ligands are being synthesized using standard synthetic techniques. Solid-phase cryptand synthesis begins by functionalizing Wang resin to obtain a reactive alkene. Next, a Michael addition is performed to add the starting cryptand material onto the resin. The final components to achieve desired cryptand are then added, followed by Hoffman elimination to cleave cryptands from resin.

**Results and Discussion:** We plan to show the current progress toward the synthesis and characterization of new fluorine-containing europium complexes, as well as the current progress towards synthesis and characterization of cryptands using solid-phase techniques.

**Conclusion:** The impact of this research is expected to improve magnetic resonance imaging relevant to hypoxia by providing the mechanistic insight and tools needed to design and synthesize new fluorous hypoxia-responsive contrast agents. Future research will be focused on synthesizing Eu<sup>II</sup> contrast agents that contain varying numbers of fluorine atoms across different ligands to enhance detection and imaging of hypoxia in vivo, and different cryptands will be synthesized using solid-phase techniques.

### References:

- 1) Fleming, I. N.; Manaki, R.; Blower, P. J.; West, C.; Williams, K. J.; Harris, A. L.; Domarkas, J.; Lord, S.; Baldry, C.; Gilbert, F. J. *Br. J. Cancer*. **2015**, *112*, 238-250.
- 2) Krohn, K. A.; Link, J. M.; Mason, R. P. *J. Nucl. Med.* **2008**, *49*, 129S-48S.
- 3) Ballinger, J. R. *Semin. Nucl. Med.* **2001**, *31*, 321-329.
- 4) Ekanger, L. A.; Mills, D. R.; Ali, M. M.; Polin, L. A.; Shen, Y.; Haacke, E. M.; Allen, M. J. *Inorg. Chem.* **2016**, *55*, 9981–9988.
- 5) Basal, L. A.; Bailey, M. D.; Romero, J.; Ali, Meser M.; Kurenbekova, L.; Yustein, J.; Pautler, R. G.; Allen, M. J., *Chem. Sci.* **2017**, *8*, 8345–8350.
- 6) Caravan, P.; Tóth, É.; Rockenbauer, A.; Merbach, A. E. *J. Am. Chem. Soc.* **1999**, *121*, 10403-10409.
- 7) Yee, E. L.; Gansow, Otto. A.; Weaver, M. J. *J. Am. Chem. Soc.* **1980**, *102*, 2278-2285.

## A new gadolinium-based contrast agent with pH-dependent relaxation properties

Md Mamunur Rashid,<sup>1</sup> Meser M. Ali,<sup>2</sup> and Matthew J. Allen<sup>1</sup>

<sup>1</sup>Department of Chemistry, Wayne State University, Detroit, Michigan, United States, <sup>2</sup>Cellular and Molecular Imaging Lab, Henry Ford Health System, Detroit, Michigan, United States.

**Introduction:** Acidic pH is a leading biomarker of malignant tumor cells;<sup>1</sup> consequently, there are several methods to image and map extracellular pH, for example, magnetic resonance spectroscopy and imaging,<sup>2–4</sup> optical imaging,<sup>5</sup> positron emission tomography,<sup>6</sup> and electron paramagnetic resonance spectroscopy.<sup>7</sup> Several of these examples involve contrast agents for magnetic resonance imaging.<sup>8</sup> To further the use of contrast-enhanced mapping of pH, we synthesized a new Gd-based contrast agent functionalized with imidazole to enable pH-dependent contrast enhancement.

**Methods:** *Synthesis:* The new complex was synthesized using standard synthetic techniques. *Relaxivity:* Solutions of the new complex were prepared in buffers ranging from pH 4 to 8. Longitudinal relaxation times were measured at 1.4 T and 37 °C. *<sup>17</sup>O-NMR studies:* <sup>17</sup>O-NMR studies were performed at pH 4.07, 5.75, and 8.03 using a Varian 400 MHz NMR instrument.

**Results and Discussions:** We incorporated an imidazole group onto a macrorocyclic ligand for Gd<sup>III</sup> because imidazole has a  $pK_a$  value relevant to physiological pH. The relaxivity of the new contrast agent significantly changes with the pH from 4 to 8 as expected, and the relaxivity at pH 4 is 2.4 times the relaxivity at pH 8. Interestingly, relaxivity at the inflection point of a plot of relaxivity vs pH decreases with time over a period of 11 days, while the relaxivity values at pH 4 and 8 are stable over the same time frame. Mass spectrometry and <sup>17</sup>O-NMR spectroscopy are being performed to study the phenomenon.

**Discussions:** We hypothesize that at pH 5.75, there are conformational changes that prevent the exchange of coordinated water, thus reducing the relaxivity. We plan to show the data characterizing the complex and how it functions.

**Conclusion:** Our Gd-based imidazole complex displays pH-sensitive relaxivity in a physiologically relevant pH range, which is expected to pique interest for further studies of the relaxation properties of the complex.

### References:

1. Botár, R.; Molnar, E.; Trencsenyi, G.; Kiss, J.; Kálmán, F.K.; Tircsó, G. *J. Am. Chem. Soc.* **2020**, *142*, 1662–1666.
2. Gallagher, F. A.; Kettunen, M. I.; Day, S. E.; Hu, D.E.; Ardenkjaer-Larsen, J. H.; Zandt, R; et al. *Nature* **2008**, *453*, 940–943.
3. Lutz, N. W.; Bernard, M. *NMR BioMed.* **2019**, *32*, e4134.
4. García-Martín, M. L.; Hérigault, G.; Rémy, C.; Farion, R.; Ballesteros, P.; Coles, J.A.; Cerdán, S.; Ziegler, A. *Cancer Res.* **2001**, *61*, 6524–6531.
5. (a) Mordon, S.; Devoisselle J. M.; Maunoury, V. *Photochem. Photobiol.* **1994**, *60*, 274–279. (b) Martin, G. R.; Jain, R. K. *Cancer Res.* **1994**, *54*, 5670–5674.
6. Frullano, L.; Catana, C.; Benner, T.; Sherry, A. D.; Caravan, P. *Angew. Chem. Int. Ed. Engl.* **2010**, *49*, 2382–2384.
7. Khramtsov, V. V.; Grigor'ev, I. A.; Foster, M. A.; Lurie, D. J.; Nicholson, I. *Cell Mol. Biol.* **2000**, *46*, 1361–1374.
8. Wahsner, J.; Gale, E. M.; Rodríguez-Rodríguez, A.; Caravan, P. *Chem. Rev.* **2019**, *119*, 957–1057.

## Towards antibody directed high-contrast MRI nanoprobes for diagnosis of Stroke

Thomas W. Price,<sup>1</sup> Zoe Booth,<sup>2</sup> Leigh Naylor-Adamson,<sup>2</sup> Hélio M. Gil,<sup>1,3</sup> Simon Calaminus,<sup>2</sup> Graeme J. Stasiuk<sup>1</sup>

<sup>1</sup> Department of Imaging Chemistry and Biology, School of Biomedical Engineering and Imaging Sciences, King's College London, St Thomas' Hospital, London, SE1 7EH, UK

<sup>2</sup> Centre for Atherothrombosis and Metabolic Disease, Hull York Medical School, University of Hull, Hull, HU6 7RX, UK

<sup>3</sup> Department of Biomedical Sciences, Faculty of Health Sciences, University of Hull, Cottingham Road, HU6 7RX, Hull, UK

**Introduction:** 100,000 people have Strokes in the UK each year. Early treatment is essential to minimise the after-effects of a Stroke; monitoring the effect of administered therapeutics would allow for adaptation of the treatment regime to optimise the clinical outcome. Traditional small molecule Gd-based contrast agents (CAs) (e.g. DOTAREM<sup>®</sup>) produce insufficient contrast to allow for effective imaging of low concentration targets such as cell receptors. The construction of multimeric, nanoscale probes has been demonstrated to improve the effective contrast both by enhancing the relaxation efficiency of the individual chelates and by increasing the local concentration of GdCAs significantly.<sup>1</sup> In this work we used nanoprobes incorporating GdCAs, fluorescent quantum dots (QDs), and antibody-based targeting, to image platelets with a view to monitoring clot formation and treatment in the future.

**Methods:** GdL<sub>1</sub>, QDs, and GdL<sub>1</sub>-QD were synthesised and characterised in line with published protocols.<sup>1,2</sup> Platelets were isolated from donor blood samples using standard protocols.<sup>3</sup> Platelet function and uptake of probe was assessed by flow cytometry, aggregometry, spreading analysis, and fluorescence microscopy.

**Results:** The chelate GdL<sub>1</sub> has an  $r_1$  of 3.25 mM<sup>-1</sup> s<sup>-1</sup> (37 °C, 400 MHz) and the nanoconstruct GdL<sub>1</sub>-QD has a per Gd  $r_1$  of 3.90 mM<sup>-1</sup> s<sup>-1</sup> (37 °C, 400 MHz), resulting in, per QD, relaxivity of 376.4 mM<sup>-1</sup> s<sup>-1</sup> (37 °C, 400 MHz). The NMRD profile of GdL<sub>1</sub> shows an increase at lower frequencies, with an  $r_1$  of 10.32 at 0.01 MHz whereas GdL<sub>1</sub>-QD has an  $r_1$  of 24.88 at 0.01 MHz, corresponding to 2400 mM<sup>-1</sup> s<sup>-1</sup> per QD (37 °C, 0.01 MHz). The shape of the NMRD profiles also differs; GdL<sub>1</sub>-QD has an additional peak in the region of 10-60 MHz which is not present for GdL<sub>1</sub>, this may further improve the clinical relevance of these nanoconstructs for providing MR contrast. A number of QD surface coatings were investigated to assess their impact on platelet behaviour: InP/ZnS QDs coated in thioglycolic acid (TGA) or Penicillamine (PEN) had minimal effect on platelet aggregation or function and showed low uptake of the QDs by the platelets at concentrations up to 30 nM in washed platelets and platelet rich plasma. QDs functionalised with antibodies through hydrophobic interactions showed no uptake in platelets and rapidly aggregated.

**Discussion:** Increasing the rotational correlation time of the GdCA by attaching well defined, stable chelates to the surface of QDs results in a 4.4 fold increase at 10 MHz and 2.7 fold increase at 60 MHz in the per Gd  $r_1$ . This improved relaxation efficiency does not take into account the potential to direct a high number of GdCAs with a single targeting motif, increasing the effective “per target” relaxivity significantly – with GdL<sub>1</sub>-QD displaying a maximum effective per QD  $r_1$  of 3203 mM<sup>-1</sup> s<sup>-1</sup> (10 MHz, 37 °C). This significant increase will make it feasible to image low concentration targets allowing for the use of MRI to diagnose a broader spectrum of maladies. The varied effect of different surface coatings on the behaviour of platelets highlights the need for thorough investigation of all aspects of nanoparticle based imaging agents. The minimal effect of TGA and penicillamine coated QDs on platelets provides an excellent platform upon which to develop this imaging technology further. The poor performance of the antibody conjugated QDs is likely due to the conjugation method used –

other approaches are under investigation which should modify the antibodies more specifically, retaining their function.

**Conclusion:** We conclude that our GdCA-functionalised QD probe, GdL<sub>1</sub>-QD, significantly increases the effective  $r_1$  compared to the small molecule GdCA GdL<sub>1</sub>. We have also shown that QD based fluorescent agents can be used to study platelets without disrupting their function. Taken together, these results lay the groundwork for the development of QD based GdCA for imaging platelets and diagnosing Stroke.

**References:** <sup>1</sup>Stasiuk, G.J., et al. Cell-Permeable Ln(III) Chelate-Functionalized InP Quantum Dots as Multimodal Imaging Agents, *ACS Nano*, **2011** <sup>2</sup>Clarke, M.T., et al. Synthesis of Super Bright Indium Phosphide colloidal Quantum Dots Through Thermal Diffusion, *Communications Chemistry*, **2019** <sup>3</sup>Yusuf, M.Z., et al. Prostacyclin Reverses Platelet Stress Fibre Formation Causing Platelet Aggregate Instability, *Scientific Reports*, **2017**

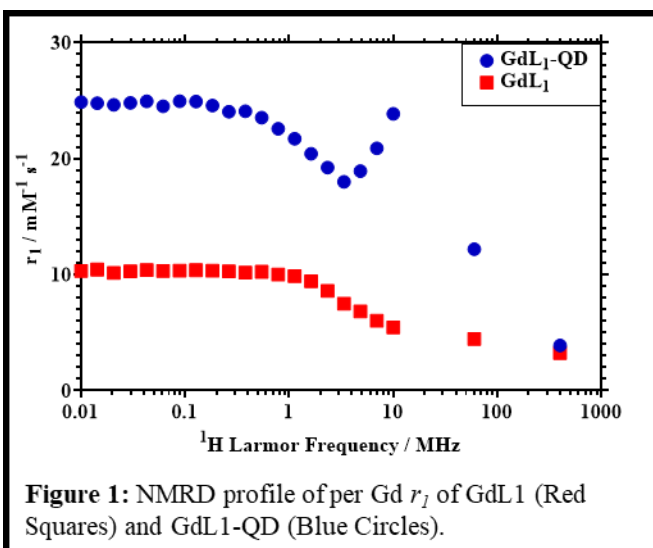


**Figure 1:** NMRD profile of per Gd  $r_1$  of GdL<sub>1</sub> (Red Squares) and GdL<sub>1</sub>-QD (Blue Circles).

# Inverted iron oxide nanoparticles with renal clearance capabilities for musculoskeletal magnetic resonance imaging

Ji-wook Kim<sup>1</sup> and Tae-Hyun Shin<sup>1</sup>

<sup>1</sup>Inventera Pharmaceuticals Inc., Seoul 08507, Republic of Korea.

**INTRODUCTION:** Iron oxide nanoparticles have been the subject of extensive studies demonstrating their potential as a magnetic resonance imaging (MRI) contrast agent. However, this agent presents several challenges due to its negative  $T_2$  contrast effects and low excretion. Recently, most of the clinical  $T_1$  contrast agents are gadolinium-based contrast agents (GBCAs), but severe side effects induced by toxic gadolinium ion such as nephrogenic systemic fibrosis are currently reported. Here, we report inverted iron oxide nanoparticles (i-IONPs) that are designed to show  $T_1$  contrast effect (Figure 1A). Due to the inverted structure of dextran core and iron oxide shell, 1) small  $r_2/r_1$  ratio and 2) fast water exchange rate which are the key factors for the  $T_1$  contrast agents are successfully achieved. In addition, the small size of i-IONP enables fast renal excretion after MR imaging. We demonstrate the feasibility of i-IONPs for musculoskeletal  $T_1$  imaging in rat animal models.

**METHODS:** *Synthesis* i-IONPs was synthesized based on our previous study<sup>1</sup>. *MRI measurement* A 9.4 T preclinical MRI system (Biospec 94/20 USR, Bruker BioSpin) with the following specifications was utilized: clear-bore size, 20 cm; gradient strength, 660 mT/m; RF amplifier power, 1,000 W; RF coil, rat body volume coil and 4-channel surface coil.

**RESULTS:** Synthesized i-IONPs have a spherical shape with an average size of about 3 nm and a narrow size distribution of <10% (Figure 1B,C). The  $r_1$  and  $r_2$  values of i-IONPs at 9.4 T MRI were measured to be 1.6 and 4.2  $\text{mM}^{-1}\text{s}^{-1}$ , respectively. The  $r_2/r_1$  ratio, a key parameter to estimate the efficiency of  $T_1$  MRI contrast agents, is 2.5, while that of ultrasmall superparamagnetic iron oxide (USPIO) is 10.0 (Figure 1D). After injection of i-IONPs into the rat knee joint (dosage, 0.25  $\mu\text{mol}$  [Fe]/ head),  $T_1$ -weighted MR images of the rat knee were significantly brightened in comparison to those of the noninjected control group. (Figure 1E). The contrast-to-noise ratio of the meniscus, capsule, cruciate, bone, and fat region are enhanced approximately 8-, 11-, 18-, 12-, 11-, and 4-fold, respectively. The contrast effects of i-IONPs are not only strong but also long-lasting: bright contrast in synovial fluid is observed for approximately 6 h postinjection (Figure 1F). For the GBCA (e.g., Dotarem)-injected group, the contrast is diminished within approximately 1 h postinjection. No iron accumulation was observed in the rat joint in the i-IONPs-injected group from Perls blue (PB) iron staining results. When we measured the cumulative urinary iron content of rats after intra-articular injection of i-IONPs, most of the intra-articularly injected i-IONPs are excreted within 24 h after injection (Figure 1G).

**DISCUSSION:** An inverted core-shell structure of a dextran core and an iron oxide shell of i-IONPs with high surface to volume ratio may provide excellent  $T_1$  contrast effects with ideally low  $r_2/r_1$ . Also, fast water exchange rate due to the exposed iron components on the surface of i-IONPs may play important role for the enhanced  $T_1$  contrast effect. The relatively long retention of i-IONPs seems to be possible because i-IONPs are approximately 40-fold larger in molecular size in comparison to Dotarem. The longlasting MRI contrast effect of i-IONPs is beneficial, as it provides an opportunity for high-resolution scanning and repeated scanning. Due to the extremely small size of i-IONPs (~3 nm), it can be excreted from the body via synovium drainage and renal clearance route.

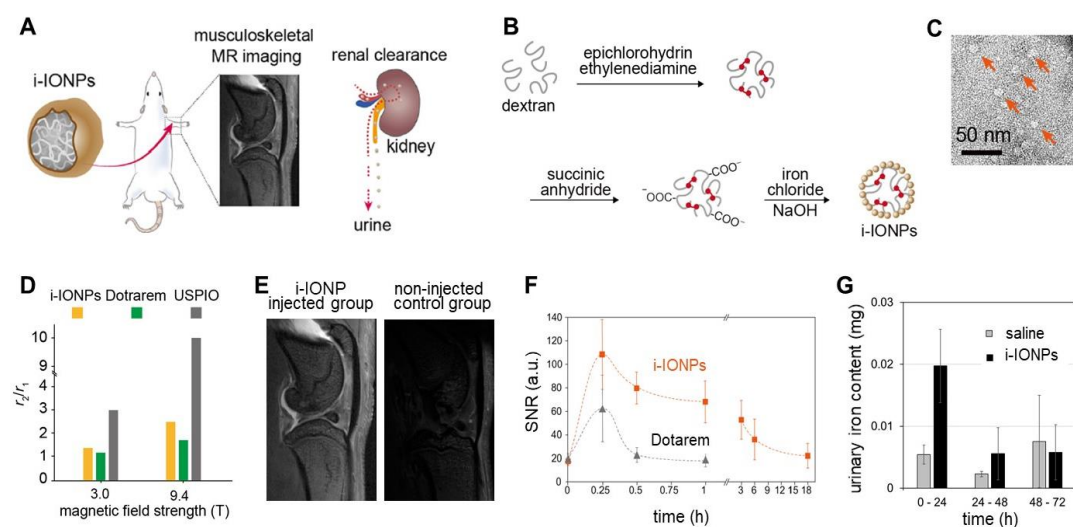


**Figure 1.** (A) Schematic illustration of i-IONPs and their application for MR arthrography. (B,C) Synthetic procedure (B) and TEM image (C) of i-IONPs. (D)  $r_2/r_1$  values of i-IONPs, Dotarem, and USPIO (E,F) In vivo MR contrast effect of i-IONPs. MR images of rat knee joints (E) and time plot of the signal-to-noise ratio (SNR) after injection of i-IONPs and Dotarem (F). (G) Cumulative urinary iron content of male rats after intra-articular injection of i-IONPs and saline.

**CONCLUSION:** Upon intra-articular injection, i-IONPs provide positive  $T_1$  and decent soft tissue contrast effects, allowing clear visualization of complex anatomical details of the joint. i-IONPs show substantially stronger and longer-lasting  $T_1$  contrast effects than conventional  $T_1$  contrast agents. In addition, i-IONPs are eliminated from the joint cavity and are safely cleared from the body through the renal clearance route. This successful demonstration of the renal clearable pharmacokinetics of intra-articularly injected i-IONPs will pave the way toward wider in vivo applicability of nanomaterials.

**REFERENCES** 1) T. H. Shin, P. K. Kim, S. Kang, J. Cheong, S. Kim, Y. Lim, W. Shin, J. Y. Jung, J. D. Lah, B. W. Choi and J. Cheon, *Nat. Biomed. Eng.*, **2021**, 5, 252–263.

## Detection and Staging of Liver Fibrosis by Precise MRI (pMRI)

Zongxiang Gui<sup>1</sup>, Oluwatosin Y. Ibhagui<sup>1</sup>, Jingjuan Qiao<sup>1</sup>, Dongjun Li<sup>1</sup>, Hua Yang<sup>2</sup>, Justin L Yu<sup>1</sup>, Shanshan Tan<sup>1</sup>, Yuguang Meng<sup>3</sup>, Shirong Wang<sup>4</sup>, Brenda-Ruth Mimba<sup>1</sup>, Bamishaye Sophia<sup>1</sup>, Francis Akinlotan<sup>1</sup>, Ravi Chakra<sup>4</sup>, Khan Hekmatyar<sup>1</sup>, Phillip Zhe Sun<sup>3</sup>, Hang Shi<sup>4</sup>, Bingzhong Xue<sup>4</sup>, Hans E. Grossniklaus<sup>2</sup>, Zhi-Ren Liu<sup>4</sup>, Jenny J. Yang<sup>1</sup>

<sup>1</sup>Department of Chemistry, Advanced Translational Imaging Facility, Center for Diagnostics and Therapeutics, Georgia State University, Atlanta, GA 30303, USA, <sup>2</sup>Department of Ophthalmology, Emory University, Atlanta, GA 30322, USA, <sup>3</sup>Yerkes National Primate Research Center, Atlanta, GA, 30329, USA, <sup>4</sup>Department of Biology, Georgia State University; Atlanta, GA 30303, USA

**Introduction:** The largest and fastest-growing population at risk for developing hepatic fibrosis are individuals with nonalcoholic fatty liver disease (NAFLD). Collagen I is highly accumulated in liver fibrosis regardless of etiology. Staging of fibrosis based on collagen I are used to decide the risk of disease progression. Our team has pioneered a new class of gadolinium-based protein contrast agents, hProCA32.Collagen, that specifically targets collagen I. In this work, we evaluated the capability of distinct molecular MR imaging with hProCA32.Collagen I and quantitative detection of both early- and late-stage non-Alcoholic fatty liver diseases (NASH) and liver fibrosis in vivo in several different mouse models including Comparative Gene Identification-58 knock out (CGI-58 KO) liver fibrosis mouse model with alteration of lipolysis, Early-stage NASH in family 1 histone deacetylase (HDAC 1) knock out, Tet KO and wild type mouse models that mimic diabetes patients.

**Methods: MRI contrast agent preparation:** hProCA32.Collagen was expressed, purified, pegylated and characterized<sup>1</sup>. **Mice models:** Early-stage fibrosis was induced in family 1 histone deacetylase (HDAC1) knock out and wild type C57BL/6 mice model (Jackson Laboratories, Bar Harbor, ME) by daily feeding with the high-fat diet with 4.2% fructose in drinking water. A more aggressive NASH and liver fibrosis model was used using CGI-58 gene

knockout mice. The other group had no CGI-58 knocked out and are therefore designated the wild type (WT) mice. **In-Vivo MRI:** All animal experiments were approved by the institutional animal care and use committee (IACUC) of Georgia State University and Emory University. Mice MRI results were acquired with a 7.0 T Bruker MRI scanner, PDFF collected during the mice generate process. T1- and T2-weighted images, and T1- and T2-mapping were collected before and after one bolus injection of hProCA32.Collagen/hProCA32 (0.025 mmol/kg) at 3, 24, and 48 hours.

**Results:** We first optimized pulse sequences and parameter for signal-to-noise ratio and sensitivity. We then evaluated the capability of hProCA32.Collagen I for in-vivo and quantitative detection of both early- and late-stage non-Alcoholic fatty liver diseases and liver fibrosis in vivo in different mouse models, taking advantage of the high r1 and r2 values. Fig. 1 show hProCA32.Collagen I and hProCA32 in CGI-58 KO mouse liver fibrosis mouse model. In contrast (Fig. 2), hProCA32 without collagen binding capability did not result in any significant enhancement observed in R1 maps at these same time points.

**Discussion:** From both Figure 1 and Figure 2, the change in R1 values calculated from T1 mapping demonstrates the highest enhancement for late-stage liver fibrosis at 3 h post-injection compared to highest enhancement for early stage observed at the 24 h time point. Change in R2 values calculated from T2 mapping shows a similar trend with the  $\Delta R1$  values, where the highest enhancement for late-stage liver fibrosis was

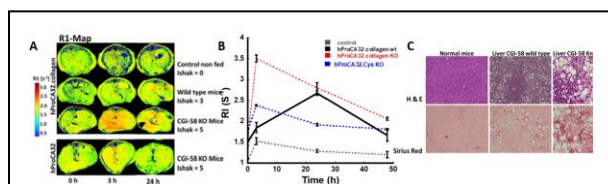


Fig. 1. R1 (A) maps with (B) R1 change of control (Ishak stage 0 of 6), wild type early-stage (Ishak stage 3 of 6), and late-stage (Ishak stage 5 of 6) of CGI58 mice model liver fibrosis before and 3 h after injection of hProCA32.Collagen and hProCA32, (C) Sirius red and H&E staining of liver tissue.

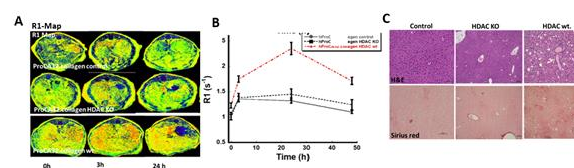


Fig. 2. R1 (A) maps with (B) R1 change of control (Ishak stage 0 of 6), wild type, (Ishak stage 3 of 6) and HDAC KO (Ishak stage 1 of 6), mice liver fibrosis model before and 24 h after injection of hProCA32.Collagen. (C) Sirius red and H&E staining of liver tissue.

observed at 3 h post-injection and at 24 h post-injection for early stage. Sirius red and H&E staining comparing early vs. late-stage fibrotic liver confirms higher collagen expression for the late stage of liver fibrosis.

**Conclusion:** The development of hProCA32.Collagen and imaging methodology enable us to detect and staging of liver fibrosis at an early stage., hProCA32.Collagen is expected to have strong application in monitoring of liver fibrosis progression, and response to treatment and facilitate to drug discovery.

**Reference:** 1) Salarian, Mani, et al. "Early detection and staging of chronic liver diseases with a protein MRI contrast agent." Nature communications 10.1 (2019): 1-14. 2) Yang, Jenny J., et al. "Rational design of protein-based MRI contrast agents." Journal of the American Chemical Society 130.29 (2008): 9260-9267.

# Development of a Fluorescence/MRI Multimodal Imaging Probe using InP and CuInS<sub>2</sub> Quantum Dots

Hélio M. Gil<sup>AB</sup>, Alina O. Muravitskaya<sup>C</sup>, Ali M. Adawi<sup>C</sup>, Simon D. J. Calaminus<sup>D</sup>, Jean-Sebastien G. Bouillard<sup>C</sup>, Graeme J. Stasiuk<sup>A</sup>

<sup>A</sup> Department of Imaging Chemistry and Biology, School of Biomedical Engineering and Imaging Sciences, King's College London;

<sup>B</sup> Department of Biomedical Sciences, University of Hull; <sup>C</sup> Department of Physics and Mathematics, University of Hull;

<sup>D</sup> Centre for Atherothrombosis and Metabolic Disease, Hull York Medical School, University of Hull.

**Introduction:** Quantum dots (QDs), have emerged as an attractive class of optoelectronic materials with increased potential for biological applications. Several studies have shown that InP/ZnS and CuInS<sub>2</sub>/ZnS (core/shell) QDs materials are safer alternatives to the traditional toxic cadmium-based nanoparticles.<sup>1,2</sup> It was also previously demonstrated that the development of multimodal probes combining QDs and Gd(III) chelates in a single agent can lead to the achievement of significantly higher MR relaxivity values and retention the fluorescent properties of the nanoparticles.<sup>3</sup> In this work we show the synthesis of InP/ZnS and CuInS<sub>2</sub> with controlled fluorescence properties in combination with Gd(III)-DOTAGA-based MRI contrast agents and analyse their multimodal imaging properties.

**Methods:** Synthesis of InP/ZnS QDs: InP/ZnS QDs were synthesized using a hot-injection method using InCl<sub>3</sub> as indium precursor and tris(diethylamino)phosphine as the phosphorous source.<sup>4,5</sup> QDs in organic phase were made water-dispersible using a phase transfer protocol with different surface ligands (thioglycolic acid, penicillamine, lipoic acid, glutathione). Synthesis of CuInS<sub>2</sub> QDs: CuInS<sub>2</sub>/ZnS QDs were synthesized *via* a water-based microwave reaction. Different parameters such as temperature, pH, core and shell growth times, Cu:In ratios and copper precursor were tested to determine optimal settings to synthesise these QDs. Synthesis of Gd-DOTAGA-based MRI contrast agents: Gd-DOTAGA was synthesized following published protocols.<sup>6</sup> Modifications on the glutamic side arm were introduced, synthesising a library of thiol-functionalised Gd(III) complexes in the side arm. Synthesis of fluorescence/MRI multimodal probe: InP/ZnS and CuInS<sub>2</sub> in water were employed in ligand-exchange protocols with the different Gd(III) complexes, thus grafting the latter on the surface of the QDs.

**Results and Discussion:** Fluorescence studies performed on synthesised InP/ZnS QDs showed concentration-dependant properties, supported by concentration-dependant lifetime measurements (Figure 1A-C). This provides important insights on how the control of the synthetic conditions of InP/ZnS QDs affects the optical properties of the nanoparticles, enabling us to define an upper limit value and validate the concentration range to use in biological experiments. For CuInS<sub>2</sub>/ZnS QDs several conditions were tested to understand how they modulate the optical properties of the final nanoparticle. Controlling the Cu:In ratio during the core growth showed a significant redshift in emission (585-705 nm) when going from 1:8 to 1:2 (Figure 1D-F). By combining these optimised fluorescent nanoparticles with different Gd-DOTAGA complexes (Figure 1A and 1D) we expect to graft 80-100 complexes to the surface of each QDs. This will allow us to obtain high relaxivity values (around 900 mM<sup>-1</sup>s<sup>-1</sup> at 35 MHz, 298 K) but also tune this relaxivity by using different linkers in the side chain that binds to the QDs.

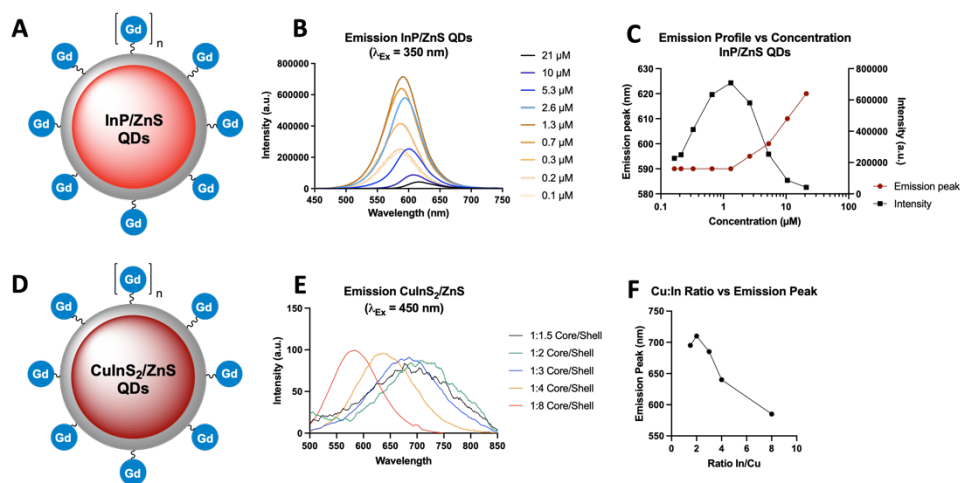


**Figure 1.** A) Schematic representation of InP/ZnS (core/shell) QDs with Gd(III) complexes (blue spheres) grafted on the surface. B) Influence of orange InP/ZnS QDs (using InBr<sub>3</sub> precursor) concentration in the emission profile. C) Variation of the emission peak wavelength and emission intensity with the real concentration of InP/ZnS QDs in hexane. Emission spectra measured at 20 °C with excitation wavelength at 350 nm. D) Schematic representation of CuInS<sub>2</sub>/ZnS (core/shell) QDs with Gd(III) complexes (blue spheres) grafted on the surface. E) Emission spectra of core/shell CuInS<sub>2</sub>/ZnS QDs with decreasing Cu:In ratio from left to right. F) Evolution of the emission peak with decreasing Cu:In ratio in CuInS<sub>2</sub>/ZnS QDs.

**References:** 1) Gil HM, et al. NIR-quantum dots in biomedical imaging and their future. *Science*, 2021, 24.3: 102189. 2) Reiss P, et al. Synthesis of semiconductor nanocrystals, focusing on nontoxic and earth-abundant materials. *Chem. Rev.* 2016, 116 (18), 10731-10819. 3) Stasiuk GJ, et al. Cell-permeable Ln (III) chelate-functionalized InP quantum dots as multimodal imaging agents. *ACS Nano*. 2011, 5 (10), 8193-8201. 4) Clarke MT, et al. Synthesis of super bright indium phosphide colloidal quantum dots through thermal diffusion. *Commun. Chem.* 2019, 2 (1), 1-7. 5) Tessier MD, et al. Economic and Size-Tunable Synthesis of InP/ZnS (E = S, Se) Colloidal Quantum Dots. *Chem. Mater.* 2015, 27 (13), 4893-4898. 6) Bernhardt C, et al. DOTAGA-Anhydride: A Valuable Building Block for the Preparation of DOTA-Like Chelating Agents. *Chem. Eur. J.*, 2012, 18.25: 7834-7841.

## Phenol-based iron(III) complexes as T<sub>1</sub> contrast agents

Roy Cineus<sup>1</sup>, Samira M. Abozeid<sup>2</sup>, Janet R. Morrow<sup>1</sup>

<sup>1</sup> Department of Chemistry, University at Buffalo, State University of New York, Amherst, NY, United States, <sup>2</sup> Department of Chemistry, Faculty of Science, Mansoura University, El-Gomhoria Street, Mansoura, Egypt.

**Introduction:** The development of iron(III) based T<sub>1</sub> contrast agents as alternatives to gadolinium T<sub>1</sub> contrast agents has been a growing field these past few years. A few examples of macrocyclic iron(III) based contrast agents from our laboratory studied in mice showed renal clearance with one agent showing a similar profile to that of gadolinium(III) based T<sub>1</sub> contrast agents.<sup>1,2</sup> Most recently, Gale et al. have reported redox and enzyme responsive iron(III) based T<sub>1</sub> contrast agents.<sup>3,4</sup> However, the development and examination of iron(III) based T<sub>1</sub> contrast agents is still in early stages. Therefore, we developed an iron(III) based contrast agent with a coordination motif of FeN<sub>3</sub>O<sub>2</sub>, where the coordinated phenol ligands can be tuned to improve solubility, study speciation, and effects on relaxivity. In addition, the effect on relaxivity upon substitution of the sixth coordinated ligand with a fluoride ion is studied towards anion responsive agents.

**Methods: Synthesis:** Ligands were synthesized using a reductive amination procedure.<sup>5</sup> The iron(III) complexes were synthesized by using ferric chloride. **Speciation:** The speciation was determined from the fitting of pH potentiometric measurements and UV-Vis spectral changes from pH titrations. All iron(III) complex solutions had an ionic strength of 0.1 M NaCl and were titrated with a known concentration of sodium hydroxide. Data collected from pH potentiometry was fit using Hyperquad software to determine binding constants and the pK<sub>a</sub> values. **Relaxivity:** A 1.4T benchtop NMR instrument is used to determine the T<sub>1</sub> times of the iron(III) complex at concentrations ranging from 0-0.6 mM. The fluoride substitution is done in situ by adding an excess of sodium fluoride to a solution of the iron(III) complex.

**Results and Discussion:** A series of six-coordinate iron(III) complexes with a triamine backbone and two pendant phenols was studied. Substituents on the phenol include methoxy, carboxy, sulfonate, pyridine and, triphenyl phosphonium. Most of the iron(III) complexes studied, have shown evidence for three different species in the pH range of 3-11. Also, an increase in the acidity of the phenolate oxygens bound to the iron(III) center leads to a decrease in the kinetic inertness of the iron(III) complex at physiological pH 7.2-7.4. The relaxivity for the iron(III) complexes fall in the range of 0.8-2 mM<sup>-1</sup>s<sup>-1</sup>. In the presence of sodium fluoride, a significant decrease in the relaxivity is observed. The decrease in relaxivity upon addition of sodium fluoride suggest that the fluoride anion is coordinating to the six-coordination site, and is disrupting inner and second sphere interactions of water protons with the iron(III) center.

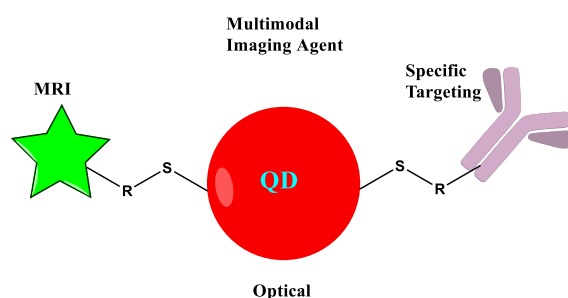
**Conclusion:** The class of iron(III) complex studied herein have tunable ionizations and some of the complexes have high aqueous solubility, which we plan to exploit to use as pH responsive and T<sub>1</sub> MRI contrast agents.

**References:**1. Snyder, E. M.; Asik, D.; Abozeid, S. M.; Burgio, A.; Bateman, G.; Turowski, S. G.; Sperryak, J. A.; Morrow, J. R., A Class of Fe(III) Macrocyclic Complexes with Alcohol Donor Groups as Effective T<sub>1</sub> MRI Contrast Agents. *Angew. Chem. Int. Ed.* **2020**, *59* (6), 2414-2419.  
2. Kras, E. A.; Abozeid, S. M.; Eduardo, W.; Sperryak, J. A.; Morrow, J. R., Comparison of phosphonate, hydroxypropyl and carboxylate pendants in Fe(III) macrocyclic complexes as MRI contrast agents. *J. Inorg. Biochem.* **2021**, *225*, 111594.  
3. Wang, H.; Wong, A.; Lewis, L. C.; Nemeth, G. R.; Jordan, V. C.; Bacon, J. W.; Caravan, P.; Shafaat, H. S.; Gale, E. M., Rational Ligand Design Enables pH Control over Aqueous Iron Magnetostructural Dynamics and Relaxometric Properties. *Inorg. Chem.* **2020**, *59* (23), 17712-17721.  
4. Wang, H.; Cleary, M. B.; Lewis, L. C.; Bacon, J. W.; Caravan, P.; Shafaat, H. S.; Gale, E. M., Enzyme Control Over Ferric Iron Magnetostructural Properties. *Angew. Chem. Int. Ed.* **2022**, *61* (3): e202114019.  
5. Abdel-Magid, A. F.; Carson, K. G.; Harris, B. D.; Maryanoff, C. A.; Shah, R. D., Reductive Amination of Aldehydes and Ketones with Sodium Triacetoxyborohydride. Studies on Direct and Indirect Reductive Amination Procedures1. *J. Org. Chem.* **1996**, *61* (11), 3849-3862.

# Multimodal imaging and guided surgery of glioblastoma using biologically-targeted quantum dots

K. Chelani, T. W. Price, M. R. Rugeiro, R. T. M. de Rosales and G. J. Stasiuk

Department of Imaging Chemistry and Biology, School of Biomedical Engineering and Imaging Sciences, King's College London, 4th Floor Lambeth Wing, St Thomas' Hospital, SE1 7EH, London, UK



## Introduction

Glioblastoma is a grade IV astrocytoma and this is known to be one of the most malignant brain cancers and are primarily diagnosed by imaging techniques such as magnetic resonance imaging (MRI) and positron-emission tomography (PET). Treatment strategies are very limited and currently the most critical strategy, alongside chemotherapy and radiotherapy is the partial resection of the tumour, where approximately 99% of tumour cells are removed; however, the progression-free survival post-surgery is relatively low. The use of fluorescent dyes for image-guided surgery (IGS) has been increasingly established due to a more 'complete' resection by better visualising the margins of the tumour; hence progression-free survival is increased.<sup>1</sup> Here, we aim to utilise biologically-compatible quantum dots (QDs), which are highly fluorescent inorganic semiconducting nanoparticles, coated with Gd-complexes for use as a dual-modal MR/fluorescent imaging probe for preoperative detection and intraoperative imaging to assist in removal of the tumour.<sup>2</sup>

## Methods

Red-emitting InP/ZnS core-shell QDs have been synthesised in organic phase and subsequently transferred into aqueous phase through a ligand exchange reaction using established protocols.<sup>3</sup> In this project, novel thiol containing Gd-DO3A based complexes were synthesised for their use as MRI contrast agents and various ligands for targeting such as prostate specific membrane antigen (PSMA) and integrins on the surface of the QD will be explored.<sup>4</sup> The QDs were characterised by measuring their optical properties and physical properties through various analytical techniques such as DLS, UV-Vis and fluorescence.

## Results

Red InP/ZnS emitting QDs are characterised to give their concentrations in a micromolar range, their hydrodynamic diameters through DLS between 5-50 nm depending on the surface ligands, and emission peak around 640 nm. Three chosen Gd-DO3A complexes synthesised were modified to optimise relaxivity properties by varying the length of the linker and introducing rigidity between the QD and the Gd chelate. Gd-1 had an  $r_1$  of  $4.67 \text{ mM}^{-1} \text{ s}^{-1}$ , Gd-2 had an  $r_1$  of  $5.85 \text{ mM}^{-1} \text{ s}^{-1}$  and Gd-3 had an  $r_1$  of  $5.76 \text{ mM}^{-1} \text{ s}^{-1}$  at 400 MHz, 298K;  $T_1$ -weighted images for these complexes were also obtained. Furthermore, both aqueous QDs and Gd-DO3A complexes were also shown to be non-toxic *in vitro* through biological assays. The Gd-DO3A complexes were conjugated to QDs through their available thiols, along with cell-targeting ligands and characterised to give  $r_1$  per QD.

## Conclusion

We will be able to discuss the potential use of QDs as multimodal imaging agents for glioblastoma using preoperative MRI and intraoperative fluorescence imaging for image-guided surgery by exploiting their versatile chemistry and unique optical properties. This work also demonstrates an optimisation strategy to maximise the MR contrast obtained using Gd functionalised QDs.

## References

1. M. E. Davis, *Clinical journal of oncology nursing*, 2016, **20**, S2-S8.
2. H. M. Gil, T. W. Price, K. Chelani, J. G. Bouillard, S. D. J. Calaminus and G. J. Stasiuk, *iScience*, 2021, **24**, 102189.
3. S. Tamang, G. Beaune, I. Texier and P. Reiss, *ACS Nano*, 2011, **5**, 9392-9402.
4. G. Stasiuk, in *Comprehensive Coordination Chemistry III*, ed. N. J. Long, Elsevier, Amsterdam, 2020, pp. 20-22.

## Redox responsive manganese-based MRI theranostics for cancer therapy

Beatriz Brito<sup>1,2,3</sup>, Maria R. Ruggiero<sup>2</sup>, Manuel Bañobre-López<sup>1</sup>, Graeme Stasiuk<sup>2</sup>, Juan Gallo<sup>1</sup>  
<sup>1</sup>Advanced (Magnetic) Theranostics Nanostructures Lab, International Iberian Nanotechnology Laboratory, Avenida Mestre José Veiga, 4715-330 Braga, Portugal  
<sup>2</sup>Department of Imaging Chemistry and Biology, School of Biomedical Engineering and Imaging Sciences, King's College London, Strand, SE1 7EH, London, UK  
<sup>3</sup>Department of Biomedical Sciences, University of Hull, HU6 7RX, Hull, UK

**Introduction:** Smart theranostics refer to dynamic platforms that integrate multiple functions, including at least imaging, therapy and responsiveness, in a single agent.<sup>1,2</sup> Different smart theranostic systems have been devised in the search for improved diagnostic and therapy efficiency, particularly in oncology, where these agents can respond to changes in the pH, redox environment, or enzymes.<sup>1,2</sup> This work describes the synthesis of MnO<sub>2</sub>-Pt nanoparticles (NPs) as redox responsive theranostics for MRI-guided delivery of Pt-based cancer therapy.

**Methods: Synthesis:** Using facile ultrasonication chemistry,<sup>3</sup> a series of Mn<sub>x</sub>O<sub>y</sub>-Pt(IV) NPs was synthesised. These NPs were thoroughly characterised by DLS, TEM, ICP, UV-vis, XPS, FTIR and XRD.

**MR Imaging:** Relaxometry studies were performed at 1.5 T and MR phantom images were acquired at clinical fields of 3.0 T. **In vitro imaging and therapeutic evaluation:** The *in vitro* MR efficiency and off-ON switchable properties of the NPs were assessed by imaging 2D and 3D cell cultures of a human lung carcinoma cell line (A549). The cytotoxicity of the NPs was assessed by means of cell viability assays in 2D and 3D cell cultures of the A549 cell line.

**Results and discussion:** The synthesis of MnO<sub>2</sub>-Pt NPs was optimised to ensure optimal switch off/ON MR properties. Relaxometry studies revealed *T*<sub>1</sub> signal enhancements as high as 136-fold for NPs with lower Pt/Mn ratios after treatment with a reducing agent, in agreement with the contrast enhancement observed in MR phantoms. Similarly, *in vitro* MRI studies on 2D and 3D cell cultures of A549 cells treated with the MnO<sub>2</sub>-Pt NPs showed a significant enhancement of the *T*<sub>1</sub> signal over 12 h, which indicates the MnO<sub>2</sub>-Pt NPs can be efficiently reduced to free Mn(II) by the cells. Results from cell viability studies show

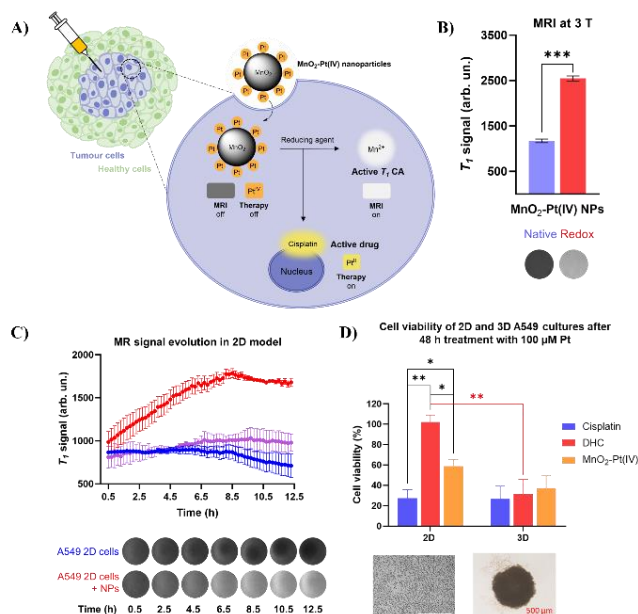


**Figure 1.** A) Proposed redox responsive mechanism of MnO<sub>2</sub>-Pt(IV) nanoparticles. B) *T*<sub>1</sub>-weighted MRI phantoms of MnO<sub>2</sub>-Pt(IV) NPs and corresponding signal before (blue) and after (red) redox treatment, [Mn] = 0.7 mM, \*\*\**p*<0.0001. C) MR *T*<sub>1</sub> signal evolution of 2D model of A549 cells treated with MnO<sub>2</sub>-Pt NPs (0.6 mM of Mn) over time, at 3 T. Blue: cells; purple: NPs in media, red: cells treated with NPs and representative *T*<sub>1</sub> images acquired. D) Comparison of cell viability in 2D and 3D A549 cell cultures after 48 h of treatment Pt concentrations of 100 μM (*n*=3), \*\*\**p*<0.005, \**p*<0.05, and representative images of 2D and 3D cell cultures used for *in vitro* imaging and cell viability studies. Scale bar represents 500 μM.

that the toxicity of the nanosystem (IC<sub>50</sub> = 100.0 μM) is considerably higher than that of the precursor Pt(IV) prodrug (IC<sub>50</sub> = 420.5 μM). Additionally, there was no significant difference in the cell viability of 3D cell models following treatment with cisplatin, the Pt(IV) prodrug and MnO<sub>2</sub>-Pt(IV) nanoparticles (100 μM of Pt), demonstrating that these more complex cell systems better resemble reductive *in vivo* tumour microenvironments.

**Conclusions:** These MnO<sub>2</sub>-Pt NPs are equipped with redox responsive imaging and therapeutic modalities. They can be reduced *in vitro* by cancer cells, leading to a significant increase of the *T*<sub>1</sub> signal. MnO<sub>2</sub>-Pt nanosystems can induce a *T*<sub>1</sub> switch as the drug is released in cancer cells, making them great candidates for image-guided drug delivery.

**References:** 1) Parodi, et al. Smart nanotheranostics responsive to pathological stimuli. *Front Bioeng Biotechnol*, **2020**, 8, 503. 2) Brito, et al. Smart magnetic resonance imaging-based theranostics for cancer. *Theranostics* **2021**, 11 (18), 8706. 3) Bañobre-López, et al. Tunable performance of manganese oxide nanostructures as MRI contrast agents. *Chem Eur J*, **2018**, 24 (6), 1295-1303.

# Imaging molecular functions in the brain with MR contrast agents

E.L. Bearer, T.W. Uselman, H.B. Gray, and R.E. Jacobs

University of New Mexico Health Sciences Center, Albuquerque, NM; Beckman Institute, California Institute of Technology, Pasadena, CA, and Zilkha Neurogenetic Institute, University of Southern California, Los Angeles, CA

Manganese-enhanced magnetic resonance imaging (MEMRI), for  $T_1$  contrast, and intravascular ultrasmall superparamagnetic particles (USPIO) for  $T_2$ , holds exceptional promise for preclinical studies of brain-wide physiology<sup>3</sup>. Physiological contrast agents report on how perturbation of specific molecules, altered either genetically or pharmacologically, effect function such as axonal transport, neural activity or cerebral blood flow (CBF).

Longitudinal MEMRI offers a powerful platform to witness functional effects of molecular perturbations, such as gene knockouts in mice. Mn(II) is powerful for two main reasons: 1) Strong effect at low doses; 2) Sensitive to biological interactions, such as projection tracing and neural activity mapping via entry into electrically active neurons in the living brain. High-spin Mn(II) reduces the relaxation time of nearby water protons: at Mn(II) concentrations typically encountered in MEMRI, robust hyperintensity is obtained without adverse effects. When delivered by stereotactic intracerebral injection, Mn(II) enters active neurons at the injection site and then travels inside axons for long distances, tracing neuronal projection anatomy. When delivered systemically, Mn(II) enters active neurons throughout the brain via voltage-sensitive calcium channels and clears slowly. Thus behavior can be monitored during Mn(II) uptake and hyperintense signals due to Mn(II) accumulation captured retrospectively, allowing pairing of behavior with neural activity maps for the first time<sup>4</sup>. Because of its independence from vascular dynamics, MEMRI may be the only method to witness effects of molecules, like cocaine, that affect both vascular and neural dynamics. We reported axonal transport dynamics in 8 different genetically altered mice with MEMRI producing clinically useful results<sup>2,5-12</sup>. USPIO are powerful for similar reasons, giving a strong effect size for measurement of CBF. One of us has reported effects CBF in living mice<sup>1,13</sup>. Automated computational processing allows data-driven, unbiased comprehensive analysis of image stacks from multiple individuals, yielding statistical significance<sup>14,15</sup>. The Bruker Biospin 11.7T MR scanner in the Beckman Institute at Caltech, and the newly updated Bruker Biospec/Avance 7T/30 cm and the Bruker BioSpec 7T/30USR at UNM's new Brain and Behavioral Health Institute, provide high resolution 4D images of living mouse brains at 100 $\mu$ m isotropic voxels over time for physiological detection of molecular effects.

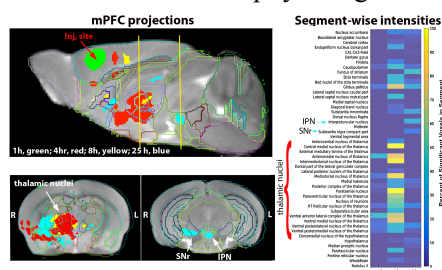


**Fig. 1. Example of MEMRI tract tracing in NET deleted mice<sup>2</sup>**

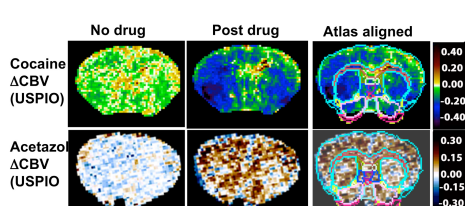


**Fig 2. Example of USPIO after cocaine<sup>1</sup>**

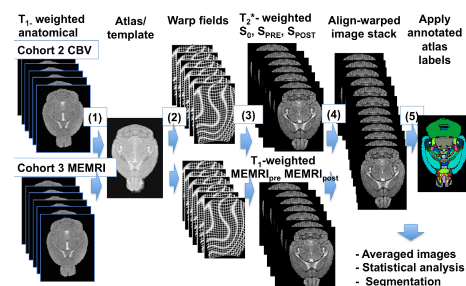


**Fig. 3. Bearer Lab computational processing steps.**

## References:

- Perles-Barbacaru, T.-A., Procissi, D., Demyanenko, A.V. & Jacobs, R.E. Quantitative pharmacologic MRI in mice. *NMR in Biomedicine* **25**, 498-505 (2012).
- Gallagher, J.J. *et al.* Altered reward circuitry in the norepinephrine transporter knockout mouse. *PLoS One* **8**, e57597 (2013).
- Uselman, T., Medina, C., Gray, H., Jacobs, R. & Bearer, E. Longitudinal manganese-enhanced magnetic resonance imaging of neural projections and activity. *NMR in Biomed* (2022).
- Uselman, T.W., Barto, D.R., Jacobs, R.E. & Bearer, E.L. Evolution of brain-wide activity in the awake behaving mouse after acute fear by longitudinal manganese-enhanced MRI. *NeuroImage* **222**, 116975 (2020).
- Bearer, E.L. *et al.* Role of neuronal activity and kinesin on tract tracing by manganese-enhanced MRI (MEMRI). *Neuroimage* **37 Suppl 1**, S37-46 (2007).
- Bearer, E.L. *et al.* Alterations of functional circuitry in aging brain and the impact of mutated APP expression. *Neurobiol Aging* **70**, 276-290 (2018).
- Bearer, E.L., Zhang, X. & Jacobs, R.E. Live imaging of neuronal connections by magnetic resonance: Robust transport in the hippocampal-septal memory circuit in a mouse model of Down syndrome. *Neuroimage* **37**, 230-42 (2007).
- Bearer, E.L., Zhang, X., Janvelyan, D., Boulat, B. & Jacobs, R.E. Reward circuitry is perturbed in the absence of the serotonin transporter. *Neuroimage* **46**, 1091-104 (2009).
- Gallagher, J.J., Zhang, X., Ziomek, G.J., Jacobs, R.E. & Bearer, E.L. Deficits in axonal transport in hippocampal-based circuitry and the visual pathway in APP knock-out animals witnessed by manganese enhanced MRI. *Neuroimage* **60**, 1856-66 (2012).
- Medina, C.S. *et al.* Hippocampal to basal forebrain transport of Mn2+ is impaired by deletion of KLC1, a subunit of the conventional kinesin microtubule-based motor. *Neuroimage* **145**, 44-57 (2017).
- Medina, C.S. *et al.* Decoupling the Effects of the Amyloid Precursor Protein From Amyloid-beta Plaques on Axonal Transport Dynamics in the Living Brain. *Front Cell Neurosci* **13**, 501 (2019).
- Zhang, X. *et al.* Altered neurocircuitry in the dopamine transporter knockout mouse brain. *PLoS One* **5**, e11506 (2010).
- Perles-Barbacaru, T.-A. *et al.* Quantitative pharmacologic MRI: Mapping the cerebral blood volume response to cocaine in dopamine transporter knockout mice. *Neuroimage* **55**, 622-628 (2011).
- Delora, A. *et al.* A simple rapid process for semi-automated brain extraction from magnetic resonance images of the whole mouse head. *J Neurosci Methods* **257**, 185-93 (2016).
- Medina, C.S., Manifold-Wheeler, B., Gonzales, A. & Bearer, E.L. Automated Computational Processing of 3-D MR Images of Mouse Brain for Phenotyping of Living Animals. *Curr Protoc Mol Biol* **119**, 29A.5.1-29A.5.38 (2017).

# Sparse Representation Learning on Magnetic Resonance Spectroscopy Imaging for Molecular Profiling of White Matter Pathologies.

Connor Sanderford, Narendiran Raghu, Catherine D Chong, Benjamin B Bartelle

## Introduction: “What is the significance of this study?”

Neurological disorders are molecular pathologies, yet clinical imaging lacks the molecular information needed to assess the underlying disease pathology for accurate diagnosis. In Multiple Sclerosis (MS), brain white matter hyperintensities (WMH), are a standard imaging marker of focal neuroinflammation detectable by MRI <sup>1</sup>. While essential to an MS diagnosis, WMHs can also be found in over 40% of migraine patients, and are a risk factor for stroke and dementia <sup>2</sup>. Lack of molecular information regarding WMH, leave them non-specific to disease.

Spatially defined molecular information of metabolites can be measured using Magnetic Resonance Spectroscopy Imaging (MRSI) <sup>3</sup>. Metabolic data is too complex to individually identify most chemical species, but it can be parsed computationally into “molecular signatures” for disease classification and validation of animal models for a given pathology. Here we define the molecular signatures of WMH associated with MS for comparison to signatures generated in preclinical models of neural lesion. Our goal is to bring molecular precision to WMH in clinical diagnosis and bridge clinical imaging with translational research.

**Methods:** We collected data from 20 female patients with MS and migraine with brain WMH using an EPI based MRSI sequence for acquisition at unprecedented scale and resolution, over 130 million data points per subject. We then developed customized “sparse learning” methods using the Pytorch libraries for Python to derive rare molecular signatures from our MRSI data <sup>4</sup>. The molecular signatures derived from our learning model are then regenerated into a representational atlas of each subjects for registration to imaging data to define MS associated WMH signatures.

**Results:** Individual subject MRSI data shows molecular signatures that track with major neuroanatomical structures, including white matter, gray matter, and sub cortical regions, demonstrating the feasibility of our method and a baseline for comparison against WMH pathologies. Next steps include combining all patient data for improved statistical analysis and tuning the parameters of our learning model based on derivation of signatures that colocalize with WMH in imaging data. With further development, this first in class analysis, can become powerful new diagnostic tool for classifying pathological tissue with molecular precision and millimeter scale resolution.

**Discussion:** Unsupervised sparse learning is already capable of classifying healthy tissue with MRSI before any optimizations. WMH features are likely present already, but are rare enough to that they must be individually identified in imaging and MRSI data and scored with a correlation analysis before a molecular signature can be confirmed. Once WMH features have been identified however, parameter tuning can maximize the informativeness of our analysis to bring this new approach to its next phases of development, validation of a preclinical model and a broader clinical study.

**Conclusion:** Sparse learning approaches offer a novel means to make full use of the MRS spectrum. One lingering issue is that, while a molecular signature is a statistically sound basis for classification, the actual chemical makeup cannot be known without extensive biochemical dissection. The current study however offers a stronger correlation between WMH and MS and offers a clear path towards improving the early diagnosis and standard of care for MS, migraine, and other WMH associated pathologies.

## References:

1. Bou Fakhredin R, Saade C, Kerek R, El-Jamal L, Khoury SJ, El-Merhi F. Imaging in multiple sclerosis: A new spin on lesions. *J Med Imaging Radiat Oncol.* 2016 Oct;60(5):577–586. PMID: 27464473
2. Chong CD, Schwedt TJ, Dodick DW. Migraine: What Imaging Reveals. *Curr Neurol Neurosci Rep.* 2016 Jul;16(7):64. PMID: 27181270
3. Nassirpour S, Chang P, Henning A. High and ultra-high resolution metabolite mapping of the human brain using 1H FID MRSI at 9.4T. *Neuroimage.* 2018 Mar;168:211–221. PMID: 28025130
4. Abbasi M, Sanderford CR, Raghu N, Bartelle BB. Improved Unsupervised Representation Learning of Spatial Transcriptomic Data with Sparse Filtering [Internet]. 2021 Oct p. 2021.10.11.464002. Available from: <https://www.biorxiv.org/content/10.1101/2021.10.11.464002v2>